Quantifying Wavelength-Dependent Plasmonic Hot Carrier Energy Distributions at Metal/Semiconductor Interfaces

Yun Yu,[†] Kanishka D. Wijesekara,[‡] Xiaoxing Xi,[‡] and Katherine A. Willets*[,†]

[†]Department of Chemistry, Temple University, Philadelphia, Pennsylvania 19122, United States

[‡]Department of Physics, Temple University, Philadelphia, Pennsylvania 19122, United States

ABSTRACT: **Hot carriers generated from the nonradiative decay of localized surface plasmons are capable of driving charge-transfer reactions at the surfaces of metal nanostructures. Photocatalytic devices utilizing plasmonic hot carriers are often based on metal nanoparticle/semiconductor heterostructures owing to their efficient electron−hole separation ability. The rapid thermalization of hot carriers generated at the metal nanoparticles yields a distribution of carrier energies that determines the capability of the photocatalytic device to drive redox reactions. Here, we quantify the thermalized hot carrier energy distribution generated at Au/TiO_2 nanostructures using wavelength-dependent scanning electrochemical microscopy and a series of molecular probes with different redox potentials. We determine the quantum efficiencies and oxidizing power of the hot carriers from wavelength-dependent reaction rates and photocurrent across the metal/semiconductor interface. The wavelength-dependent reaction efficiency tracks the surface plasmon resonance spectrum of the Au nanoparticles, showing that the reaction is facilitated by plasmon excitation, while the responses from molecules with different redox potentials shed light on the energy distribution of the hot holes generated at metal nanoparticle/semiconductor heterostructures. The results provide important insight into the energies of the plasmon-generated hot carriers and quantum efficiencies of plasmonic photocatalytic devices.**

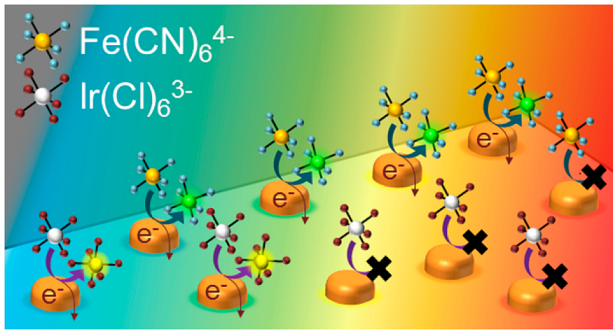

KEYWORDS: *plasmon, hot-hole, hot carriers, photoelectrochemistry, Fermi−Dirac, SECM*

Metallic nanoparticles have attracted significant interest due to their tunable optical properties coupled with catalytic activities that support light-chemical reactions.[1−7] The nonradiative decay of localized surface plasmons, *i.e.*, collective oscillations of the conduction electrons upon light stimulation, results in the generation of hot charge carriers with energies above the Fermi energy of the metal, which participate in subsequent chemical reactions.[8−11] The major limitations on the photocatalytic efficiency of plasmon-excited hot charge carriers are the rapid recombination of the electrons and holes that prevent successful extraction as well as the loss in carrier energy due to carrier scattering within the plasmonic metals. Metal/semiconductor heterostructures are recognized to overcome the former challenge and facilitate charge separation by forming an interfacial energy barrier, thus efficiently extending the lifetimes of the hot carriers generated from plasmon decay.[1,12,13] The charge accumulation at the plasmonic structures and semiconductors allows a variety of charge-transfer reactions to occur, such as water splitting,[14−18] CO_2 reduction,[19,20] and oxidation of organic molecules.[21,22] A typical metal/semiconductor structure consists of plasmonic nanoparticles in contact with an electron-transporting semiconductor (*e.g.*, TiO_2) and the Schottky barrier formed between them.[12] Hot electrons with energies higher than the Schottky barrier energy are injected into the conduction band of the semiconductor, and the plasmonic nanoparticles are left positively charged. The accumulated holes can transfer to electron-donors in solution to maintain charge balance, thus driving photoelectrochemical oxidation reactions. Extensive research effort has been dedicated to exploring the fundamentals and applications of these types of photocatalytic devices.[13,14,21,23−27]

The quantum efficiencies of the metal/semiconductor devices that exploit surface-plasmon generated hot carriers are typically too low for practical applications. One factor that

impacts the photochemical efficiency is the energy level of the hot carrier relative to that of the reactant molecule. The energy diagram in Figure 1 depicts possible charge transfer

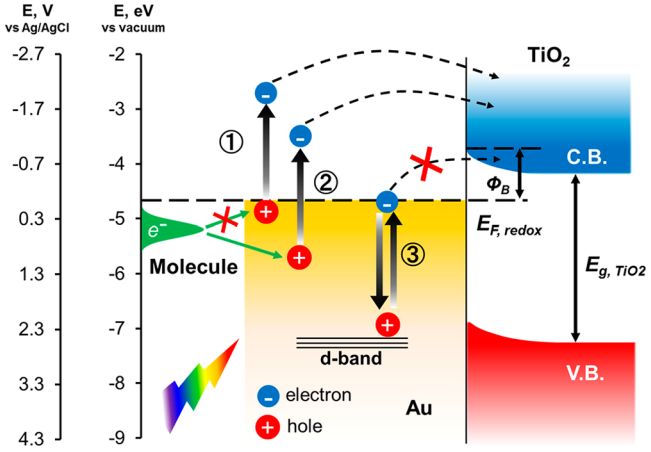

Figure 1. Energy diagram depicting hot carrier generation and charge transfer mechanisms. (1) Holes generated near the Fermi level ($E_{F,redox}$) have insufficient energy for charge transfer. (2) Holes with a suitable energy allow both charge transfer and charge separation. (3) Generation of energetic holes result in electrons having insufficient energy to be injected to TiO_2.

mechanisms in an Au/TiO_2 system. (1) Generation of highly energetic electrons allows electron injection into the TiO_2 and thus efficient separation of electron–hole pairs. However, charge transfer to a nearby molecule is prevented if the resultant hole energy is less negative than the highest occupied molecular orbital (HOMO) level of the redox molecule. (2) When an electron with a lower energy is excited, charge separation is still achievable as long as the electron energy overcomes the Schottky barrier, Φ_B. The generated hole has sufficient energy to transfer into the HOMO of the molecule, thus driving the photoelectrochemical oxidation. (3) The production of holes with very negative energy levels (*e.g.*, at the edge of the d band) results in the excited electrons having insufficient energies to overcome the Schottky barrier, leading to fast carrier recombination and diminished photo-oxidation rate.

The situation is further complicated by the fact that the energetic electrons and holes undergo rapid thermalization (<100 fs), creating a distribution of hot carrier energies that depend on the size of the plasmonic nanoparticles, the incident photon energy, the charge carrier lifetime, and the band structure of the semiconductor.[6,8,28,29] Knowledge about the number of carriers with suitable energies to be transferred to certain redox molecules allows the quantum efficiency of a photoelectrochemical reaction to be more predictive. Although appropriate theoretical frameworks have been developed[29−31] and spectroscopic techniques have been carried out[32] to describe the energy distribution of plasmon-induced hot carriers, direct experimental quantification of hot carrier energies from plasmon-driven photoelectrochemistry at a metal/semiconductor structure remains missing. The roles of carrier energy are often convoluted with other factors that can affect the apparent rate of the reaction, such as light absorption, charge separation efficiency, and electron-transfer kinetics.

In this report, we probe the distribution of hot carrier energies at a plasmonic nanoparticle/semiconductor substrate (Au/TiO_2) using wavelength-dependent scanning electrochemical microscopy (SECM) and a series of molecular

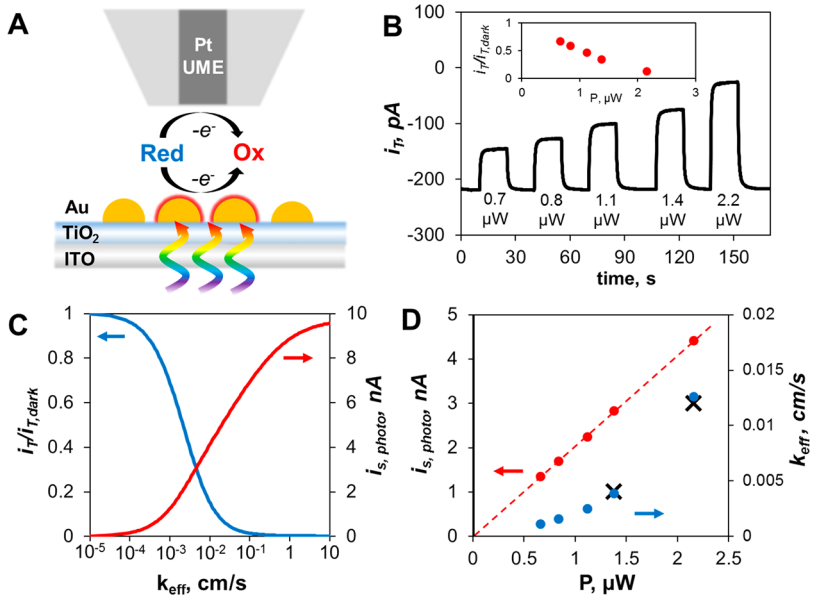

Figure 2. (A) Schematic representation of an SECM competition experiment, in which light drives oxidation at the substrate electrode and an electric potential drives the same reaction at the UME tip. (B) Tip current (i_T) *vs* time trace obtained with an 820 nm radius Pt tip placed 10 μm away from the Au/TiO_2/ITO substrate as 585 ± 18 nm excitation is turned on and off. The illumination power during the times when the light is on are indicated in the figure. The inset shows $i_T/i_{T,dark}$ as a function of power. The solution contains 1 mM $Fe(CN)_6^{4-}$ and 0.5 M KCl. Tip electrode is biased at 0.4 V *vs* Ag/AgCl, and the substrate is at open circuit. (C) Simulated calibration curves correlating $i_T/i_{T,dark}$, $i_{s,photo}$, and k_{eff} as obtained by a diffusion model. (D) Plots of substrate photocurrent (red points) and k_{eff} (blue points) *vs* the light power extracted from the data in panel B. k_{eff} obtained from independently measured SECM approach curves (Figure S3) are shown as black × to validate the model.

probes with varying redox potentials. SECM has been previously employed for probing the dynamics of a variety of photoelectrochemical processes,[33−38] including surface-plasmon enhanced charge-transfer reactions.[36−38] In an SECM experiment, an ultramicroelectrode (UME, <1 μm) employed as a tip is positioned close to a region of interest of a substrate, as depicted in Figure 2A. The hot-hole induced photo-oxidation reaction at Au nanoparticles results in the conversion of redox molecules from their reduced form (*Red*) to their oxidized form (*Ox*), thus decreasing the concentration of *Red* near the substrate surface. Measuring the current associated with the electrochemical oxidation of *Red* at the tip electrode allows us to monitor its local concentration change and thus the photoelectrochemical dynamics at the plasmonic substrate. The apparent reaction rate and the reactant flux across the illuminated substrate (*i.e.*, photocurrent) can be extracted from the tip current response with the help of a diffusion model. By normalizing the photocurrent by the incident photon flux, we can readily obtain the quantum efficiency of a photochemical reaction that is free from the interference from side reactions, such as water oxidation.[14] Furthermore, we choose outer-sphere electron-transfer molecules as the redox probes. Unlike catalytic reactions that are often sluggish and sensitive to the charge-transfer interface, the kinetics of the outer-sphere electron-transfer reactions are generally very rapid,[39] thus allowing the measured reaction rate and quantum efficiency to be largely determined by the energy of the hot carriers. We explore the effects of the excitation wavelength and the redox potential of the molecules on the photoelectrochemical reaction rate using SECM. The wavelength and redox probe dependent quantum efficiencies provide insights into the reactivity and energy distribution of the hot-holes generated by surface-plasmon decay.

RESULTS AND DISCUSSION

We fabricate Au/TiO_2/indium tin oxide (ITO) heterostructures as metal/semiconductor samples. A uniform thin film of amorphous TiO_2 with thickness of ∼40 nm (Figure S1) is deposited onto a conductive ITO coated glass coverslip by pulsed laser deposition (PLD)[40] (see the Methods section for details). Au nanoparticles are assembled onto the surface of the TiO_2/ITO by thermal evaporation deposition. Closely packed individual Au disks with diameters ranging from 20 to 60 nm (Figure S1C) are formed after 1 h annealing in air.

For photoelectrochemical experiments, the incident light is introduced from a broadband white light source to the bottom of the substrate through a 60×/1.45 NA objective. Band-pass filters and neutral-density filters are placed in the optical path to modulate the excitation wavelength and power, respectively. The beam is focused at the sample with a spot size of ∼80 μm in diameter and drives the photoelectrochemical reactions only at the illuminated portion of the substrate. The maximum excitation power used in the experiments is ∼20 μW, corresponding to an intensity of ∼1 W/cm^2. The temperature increase at this illumination intensity is expected to be <0.1K based on our previous work,[37,38] and thus photothermal heating effects on the electrochemical response is negligible. Our previous work on a Au/ITO substrate showed plasmon-driven photo-oxidation at the gold nanoparticles, with the hot electrons injected into the weakly n-type ITO substrate.[37] In this system, we observe similar photo-oxidation at the gold, with the hot electrons injected into the underlying TiO_2 hole transport layer, leaving hot holes available for electrochemical oxidation.

We first perform experiments using a one-electron-transfer, reversible redox molecule, $Fe(CN)_6^{4-}$ (the reduced form, *Red*). The solution contains 1 mM $Fe(CN)_6^{4-}$ and 0.5 M supporting electrolyte, KCl. Plasmon excitation and hot carrier generation leads to the following photochemical reaction taking place at the Au/electrolyte interface:

$$Fe(CN)_6^{4-}(Red) - e^- \xrightarrow{k_{eff}} Fe(CN)_6^{3-}(Ox) \quad (1)$$

where k_{eff} is the apparent rate constant. A potential of 0.4 V *versus* Ag/AgCl is biased at the Pt UME used as the tip electrode, corresponding to electro-oxidation of $Fe(CN)_6^{4-}$ at a diffusion-controlled rate (Figure 2A). The steady-state diffusion limiting current at the tip ($i_{T,\infty}$) obtained at this potential is proportional to the local concentration of $Fe(CN)_6^{4-}$, as given by eq 2 below,[41]

$$i_{T,\infty} = 4FD_RC_Ra \quad (2)$$

Here, F is the Faraday constant, a is the radius of the tip electrode, and D_R and C_R are the diffusion coefficient and the concentration of $Fe(CN)_6^{4-}$ respectively. The magnitude of $i_{T,\infty}$ provides direct information on the local concentration of the redox molecules.

First, we operate the SECM in competition mode, *i.e.*, the oxidation reaction proceeds at both the tip electrode and substrate, and the tip current reports the consumption rate of *Red* at substrate (Figure 2A). An 820 nm-radius tip was positioned 10 μm away from the substrate and the current at the tip electrode (i_T) was measured as a function of the excitation power (P). The time trace of i_T recorded while 585 ± 18 nm excitation light was modulated is shown in Figure 2B. The tip current was originally 219 pA under dark conditions, corresponding to the local concentration of $Fe(CN)_6^{4-}$ identical to the bulk. Upon 0.7 μW excitation, the magnitude of i_T quickly drops and levels off at 148 pA, suggesting that the local $Fe(CN)_6^{4-}$ concentration decreases due to photo-oxidation at the plasmonic substrate. i_T returns to the baseline current when the light is turned off ($i_{T,dark}$), reflecting the rapid charge transfer and diffusion of the redox molecules within the tip−substrate gap that allows a steady-state response to be readily attained.[35−37] As the light is modulated with increasing excitation intensity, the magnitude of i_T relative to the dark current ($i_T/i_{T,dark}$) further decreases (Figure 2B and inset), suggesting increased oxidation rates at the Au/TiO_2/ITO substrate under higher illumination power. Generation-collection SECM experiments (*i.e.*, photo-oxidation at the substrate and electro-reduction at the tip) were carried out to quantify the production rate of $Fe(CN)_6^{3-}(Ox)$ (Figure S2), yielding results that agree with Figure 2B. The observed photo-oxidation reaction at Au/TiO_2/ITO suggests that the conductive substrate (*i.e.*, ITO) helps clear away the accumulated electrons at the illuminated area even without a connection to the external circuit.

To quantify the photoelectrochemical reaction rates at the plasmonic substrate, we developed a diffusion model (details in SI) to extract kinetic parameters from our experimental data. Briefly, we vary the effective rate constant of the light-driven photoelectrochemical reaction at the substrate (*e.g.*, eq 1), then calculate the resulting concentration profile and diffusive flux of the redox molecules to the tip in order to extract i_T. Figure 2C (blue curve) shows how the calculated $i_T/i_{T,dark}$ changes as

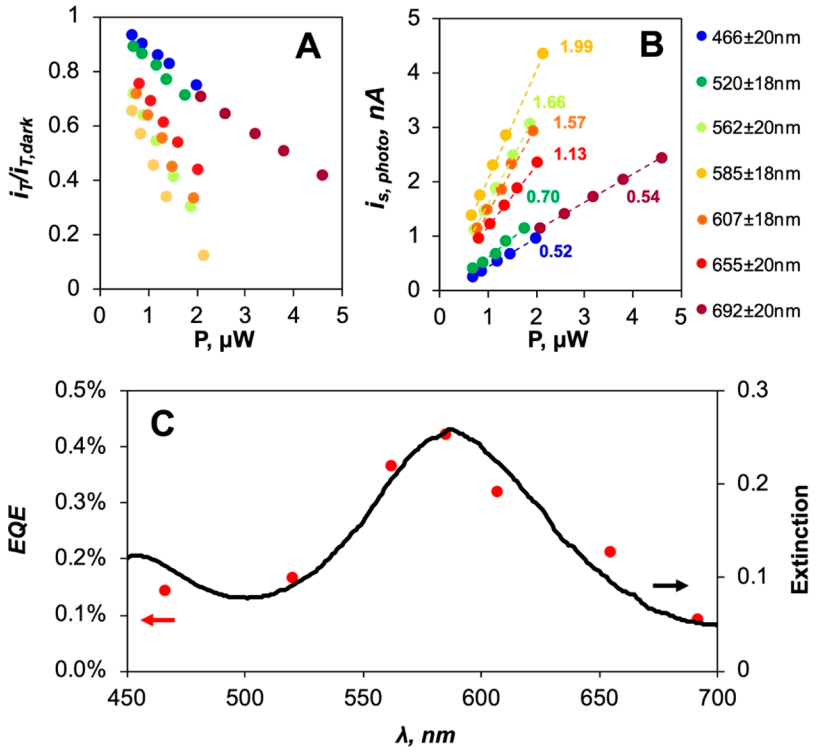

Figure 3. Plots of $i_T/i_{T,dark}$ (A) and extracted substrate photocurrents (B) *vs* the light power under excitation with different wavelengths. The slopes (nA/μW) of the linear fits are shown next to each curve in panel B. (C) Action spectra of external quantum efficiencies (EQE, red), and the extinction spectrum of the Au film (black).

a function of the apparent rate constant, k_{eff}. A lower $i_T/i_{T,dark}$ value corresponds to a higher k_{eff}, as expected (*e.g.*, faster oxidation kinetics at the substrate leads to a lower concentration of *Red* available to react at the tip and thus a corresponding decrease in i_T). By calculating the integrated diffusion flux of the molecules across the entire illuminated substrate in the model, we also evaluate the substrate photocurrent ($i_{s,photo}$) at different k_{eff}, as shown in the red curve in Figure 2C. The photocurrent at the substrate becomes larger as the reaction rate increases, and eventually reaches the diffusion-limited region at very high k_{eff}. One can find that the suitable working range lies between $k_{eff} = 10^{-4}$–0.1 cm/s. This model allows an indirect evaluation of the current flowing at the substrate without a potential bias. The substrate photocurrent extracted in this way is determined solely by the redox process of interest, and is free from the interference of concurrent side reactions, such as water oxidation.

Using the calibration curves in Figure 2C, we converted the tip current data in Figure 2B to values of k_{eff} and $i_{s,photo}$ under different illumination powers. The power dependent effective rate constants are shown as blue points in Figure 2D. To verify the reliability of this model in quantifying the reaction kinetics, we perform SECM feedback experiments and fit current-distance curves in order to independently determine k_{eff} (Figure S3). The values of k_{eff} extracted from the SECM feedback experiments are plotted as black points in Figure 2D, and show excellent agreement between the kinetic parameters obtained from the two independent experiments, validating the approach.

The extracted substrate photocurrent (red points in Figure 2D) shows a linear relationship with excitation power, with a *y*-intercept of zero as expected. We determine the external quantum efficiency (EQE) of the photo-oxidation reaction, *i.e.*, the ratio of the electron flux to the incident photon flux, from the slope of the linear fit to these data using eq 3,

$$\mathrm{EQE} = \frac{i_{s,\mathrm{photo}}/e}{P/h\nu} \tag{3}$$

where $i_{s,photo}/P$ is the slope (current/power), e is the charge of one electron, and $h\nu$ is the photon energy. The slope value of 1.99 nA/μW obtained from Figure 2D is equivalent to an EQE of 0.42%, similar to that reported in most studies using the same photocatalytic device.[17,26,42] We note that this EQE is a lower bound, due to the possibility of hot electrons injected into the exposed TiO_2 layer converting the $Fe(CN)_6^{3-}$(*Ox*) produced at the gold back to the $Fe(CN)_6^{4-}$(*Red*) form.

We next investigate the wavelength dependence of the photoelectrochemical oxidation rate of $Fe(CN)_6^{4-}$. A broad excitation wavelength range (466–692 nm) was chosen to overlap the extinction spectrum of the Au. The $i_T/i_{T,dark}$ responses measured under different excitation powers at each wavelength (λ) are shown in Figure 3A. The substrate photocurrents were obtained using the calibration curve from our diffusion model (Figure 2C) and plotted as a function of power in Figure 3B. The linear relationships of photocurrent *vs* power show different slopes, indicating that the quantum efficiencies of the photoelectrochemical reaction are wavelength dependent. We compared the wavelength dependence data with the extinction spectrum of the Au, which is obtained using eq 4,

$$\mathrm{extinction} = -\log_{10}\left(1 - \frac{I_1 - I_2}{I_0}\right) \tag{4}$$

where I_0, I_1, and I_2 are the incident light intensity, and the transmitted light intensities through TiO_2/ITO and Au/TiO_2/

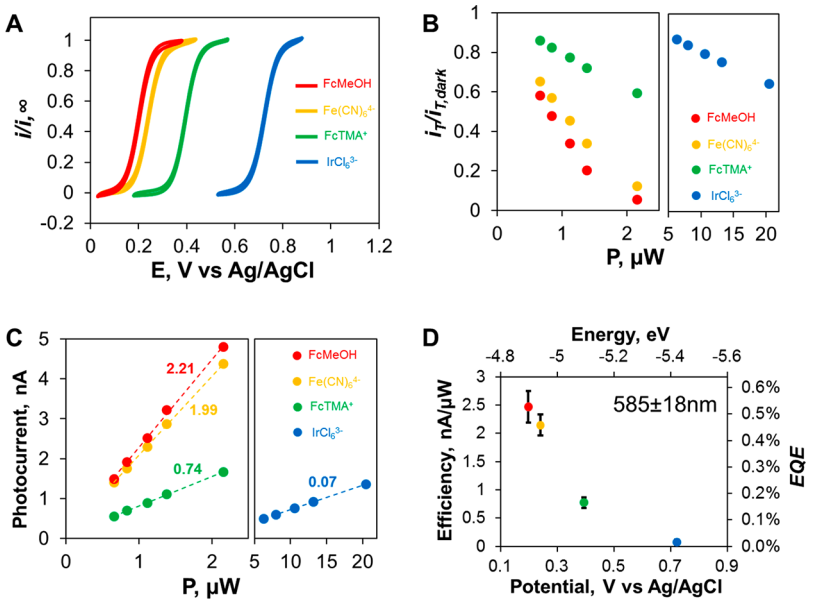

Figure 4. (A) Steady-state voltammograms of FcMeOH (red), $Fe(CN)_6^{4-}$ (orange), $FcTMA^+$ (green), and $IrCl_6^{3-}$ (blue) normalized by the diffusion limiting currents. Plots of $i_T/i_{T,dark}$ (B) and extracted substrate photocurrents (C) *vs* the light power using the different redox mediators. The tip electrode potentials are 0.35 V (red), 0.4 V (orange), 0.6 V (green), and 0.9 V (blue) *vs* Ag/AgCl, respectively. The excitation wavelength is 585 ± 18 nm. (D) Plot of the quantum efficiencies *vs* the HOMO energy levels of each mediator.

ITO respectively. As shown in Figure 3C, the action spectra of the EQE (red) qualitatively matches with the extinction spectrum of the Au nanoparticles (black). The highest efficiency is obtained using 585 ± 18 nm excitation, consistent with the plasmon-resonance peak observed at ~590 nm in the extinction spectrum. This confirms that the charge-transfer originates from the hot carriers generated from the decay of localized surface plasmons in the Au. Experiments performed on a different $Au/TiO_2/ITO$ sample yield consistent wavelength dependent data (Figure S4).

The extinction spectrum of bare TiO_2 shown in Figure S5 suggests that no direct bandgap excitation by visible light is in play. To further verify that the Au nanoparticles are responsible for the hot carrier generation, we performed control experiments on a bare TiO_2/ITO substrate and found the change in i_T is 1−2 orders of magnitude lower than that obtained with an $Au/TiO_2/ITO$ sample under the same irradiation conditions (Figure S6). The negligible change in i_T obtained with an Au/ITO sample suggests an extremely low efficiency due to rapid charge recombination in the absence of a semiconductor layer.

Next, we discuss the effects of hot carrier energy on photoelectrochemical reactions. As depicted in Figure 1, the least negative energy of a generated hole is E_F, where the value of E_F is determined by the redox molecules present in the solution.[1,43] Open-circuit potential measurements (Figure S7) show that E_F is at ~0 V *vs* Ag/AgCl (−4.7 eV *vs* vacuum). The minimum electron energy required for electron injection to the TiO_2 layer is $E_F + \Phi_B$, where Φ_B = ~1.1 eV[18] is the Schottky barrier formed at the Au/TiO_2 interface. The most negative energy level of a hole that still allows electron injection into the semiconductor and efficient charge separation is $E_{max} = E_F + \Phi_B - h\nu$. Taking 585 nm excitation as an example, the photon energy $h\nu$ = 2.12 eV yields an E_{max} = −5.72 eV *vs* vacuum (1.02 V *vs* Ag/AgCl). If the hole energy is more negative than E_{max}, the excited electron has insufficient energy to overcome the Schottky barrier and leads to charge recombination. Thus, the energy of the photogenerated holes available for driving charge transfer reactions lie in the range between E_F and E_{max}. However, the holes produced upon initial photoexcitation also undergo internal collisions and lose energy, the result of which is that most holes have energies closer to E_F (less oxidizing power) than E_{max} (more oxidizing power).

Our objective is to extract the energy distribution of the hot holes in $Au/TiO_2/ITO$ samples by quantifying the number of hot charge carriers with sufficient oxidizing power to drive charge transfer reactions in probes with varying redox potentials. To choose the probes for these studies, we need redox reactions with well-defined standard potentials, simple reaction mechanisms (*e.g.*, one electron transfer), and rapid electron-transfer kinetics. Catalytic reactions used in most studies on plasmonic photoelectrochemistry[4,12] are often sluggish and sensitive to the catalyst surface, which introduce additional uncertainties in extracting hot carrier energy information from the apparent reaction rate. In this work, we choose ferrocenemethanol (FcMeOH), ferrocyanide ($Fe(CN)_6^{4-}$), ferrocenyl methyl trimetylammonium ($FcTMA^+$), and hexachloroiridate(III) ($IrCl_6^{3-}$) as redox probes. The oxidation of these molecules proceeds in one-electron-transfer, outer-sphere mechanisms with rapid kinetics.[41,44,45] The apparent reaction rate is therefore dominated by the energy of the generated hot holes relative to the redox potential of these molecules. In addition, these molecules are chosen to avoid strong absorption of visible light near the plasmon resonance peak of the substrate (Figure S8). The HOMO levels of these molecules can be estimated from the half-wave potentials (potential at half of the limiting current plateau) in their steady-state voltammograms,[39] as shown in Figure 4A. The determined HOMO levels of FcMeOH, $Fe(CN)_6^{4-}$, $FcTMA^+$, and $IrCl_6^{3-}$ are 0.198, 0.241, 0.395, and 0.723 V *vs* Ag/AgCl, corresponding to −4.9, −4.94, −5.1, and −5.42 eV *vs* vacuum, respectively. A more negative value of the HOMO energy (in eV) reflects that the probe is increasingly difficult to oxidize.

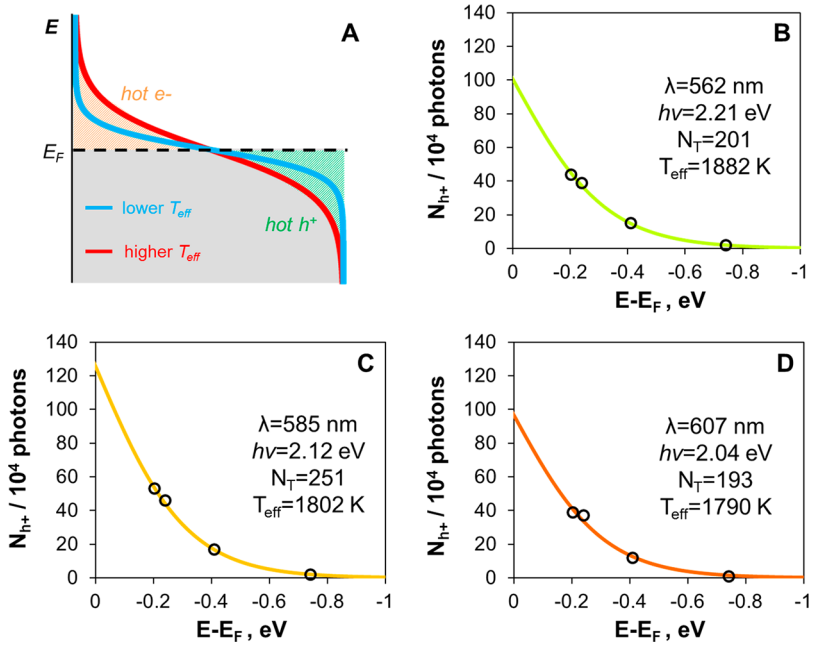

Figure 5. (A) Schematic representation showing that the carrier distribution thermalizes to an elevated effective temperature, T_{eff}. Hot electrons are represented by the orange areas above the E_F and hot holes are represented by the green area below E_F. (B–D) The hole populations obtained from the probe dependent experiments (black symbols) fit to eq 5 with the excitation wavelengths of 562 ± 20 nm (B), 585 ± 18 nm (C), and 607 ± 18 nm (D). The results of the fits are shown in each panel.

We use 585 ± 18 nm light matching the plasmon resonance peak of Au to excite the Au/TiO_2/ITO sample. Each redox solution contains 0.5 M KCl as supporting electrolyte and 1 mM redox species. The tip electrode was biased at 0.35, 0.4, 0.6, and 0.9 V *vs* Ag/AgCl to drive electrochemical oxidation of FcMeOH, $Fe(CN)_6^{4-}$, $FcTMA^+$, and $IrCl_6^{3-}$, respectively, at their diffusion controlled rates (as shown schematically in Figure 2A). The $i_T/i_{T,dark}$ responses obtained under varying radiation powers are shown in Figure 4B. Calibration curves accounting for different diffusion coefficients of each probe were created to extract $i_{s,photo}$ from $i_T/i_{T,dark}$. The determined substrate photocurrents are plotted as a function of power in Figure 4C. The highest slope of the linear fit (2.21 nA/μW) is obtained with FcMeOH, corresponding to an EQE of 0.47%, slightly higher than that of $Fe(CN)_6^{4-}$(0.42%), which is consistent with the observation that FcMeOH has a more positive HOMO and is therefore easier to oxidize. The efficiency obtained with molecules with more negative HOMO energies are even lower (0.16% for $FcTMA^+$, and 0.01% for $IrCl_6^{3-}$). The same probe-dependent experiments were performed using a different Au/TiO_2/ITO sample fabricated under the same conditions. The average quantum efficiencies obtained from the two independent measurements are plotted as a function of the HOMO energy of the probes in Figure 4D. The measured quantum efficiency of photo-oxidation shows a clear decrease as the molecules become increasingly more difficult to oxidize, as expected. The EQE *vs* energy curves obtained with excitation using other wavelengths close to the plasmon resonance peak are shown in Figure S9, which qualitatively resemble the data in Figure 4D.

To understand these data, we must consider how plasmon-excited hot carriers drive photoelectrochemical reactions. While the initial excitation event generates hot electrons and holes with energies well above and below the Fermi energy of the material, respectively, these hot carriers undergo electron–electron/hole–hole collisions within 10–100 fs of excitation, leading to a distribution of hot carrier energies. This distribution can be qualitatively described by an elevated hot carrier temperature, which decays rapidly as the hot carriers undergo further collisions.[31] At longer time scales (>100 fs), the hot carriers interact with the phonon modes of the material, further decreasing the energies of the hot carriers, while increasing the lattice temperature of the material.[7] Although the carriers are losing energy continuously, it is convenient to use a two temperature model to describe the two regimes: the elevated hot carrier temperature at short time scales (10–100 fs) and the elevated lattice temperature at longer time scales (>100 fs).[7] While the latter regime is well described by Fermi–Dirac statistics, the former regime shows deviations from this statistical description, especially at the shortest time scales, with significant populations of hot holes and electrons with energies well outside the thermalized distribution.[31] However, because we are performing our measurements under continuous wave excitation, it is impossible to know at what point in time our molecular probes are harvesting charge carriers at the nanoparticle surface. Thus, in our subsequent discussion, we will apply Fermi–Dirac statistics to our data analysis with the caveat that the extracted temperatures (called an effective temperature below) are most likely lower bounds for the elevated charge carrier temperature.[7]

Beyond considering the distribution of hot carrier energies, we must also consider the efficiency with which the hot carriers are harvested by the molecular probes. Presumably, there are far more hot carriers generated inside the nanoparticle that have sufficient energy to oxidize our probes than are actually extracted by the molecules. By choosing outer sphere probes, we do not require an interaction between the molecule and the electrode, while also allowing faster charge transfer than the inner sphere probes that are often used for hot carrier photocatalysis. In principle, this should produce higher extraction yields, although experiments to verify this

hypothesis are in progress. Similarly, the size of the nanoparticle will also impact the probability that hot carriers with sufficient energy to drive oxidation/reduction make it to the nanoparticle surface.[31] Thus, we point out that the EQEs we reported above, and used in our subsequent analysis, do not reflect the absolute number of plasmonic hot carriers with energy above a certain threshold, but are rather the number of hot carriers that are extracted by our molecular probes. From a device perspective, the latter value is the more important of the two, because it directly reports whether productive chemistry is accomplished by the plasmon-driven hot carriers.

If we now consider our data, we first recognize that the HOMO level of a molecule relates to the energy required to remove an electron from the molecular orbital. Molecules with a less negative HOMO level (*e.g.*, near E_F) allow more of the holes generated by plasmon excitation/thermalization to take part in the charge transfer reaction, while fewer holes are energetically accessible to those molecules with a more negative HOMO level (*e.g.*, closer to E_{max}). For instance, the average EQE of 0.53% obtained with FcMeOH indicates that 53 holes were extracted with energies more negative than the HOMO level of this redox molecule (−4.9 eV *vs* vacuum) upon excitation by 10^4 incident photons, while an EQE of 0.17% obtained with FcTMA suggests that 17 holes were extracted with energies more negative than −5.1 eV *vs* vacuum. The quantum efficiencies obtained from the different molecules with specific redox potentials therefore shed light on the quantity of holes available over a given range of energies.

As discussed previously, the initially excited energetic carriers undergo rapid thermalization and yield a distribution of hot carrier energies, which is reflected in the oxidation potential dependence of the EQEs shown in Figures 4D and S9. As discussed above, Fermi−Dirac statistics provide a window into the effective temperature of the hot carrier distribution, with a hotter effective temperature reflecting a larger number of hot holes with higher oxidizing power (as shown schematically in Figure 5A).[6,8] The number of holes (N_{h+}) with an energy at or below energy E, can be described by the Fermi−Dirac distribution function shown in eq 5,[31]

$$N_{h+}(E) = N_T\left[1 - \frac{1}{1 + e^{(E-E_F)/kT_{eff}}}\right] \quad (5)$$

where N_T is the total number of generated holes, E_F is the Fermi level (−4.7 eV *vs* vacuum), k is Boltzmann's constant (8.62×10^{-5} eV/K), and T_{eff} is the effective carrier temperature discussed above. We fit the N_{h+} data obtained from Figure 4D and Figure S9 to eq 5, where N_T and T_{eff} are the adjustable parameters. Figure 5B shows the number of extracted holes (N_{h+}) per 10^4 incident photons (562 ± 20 nm) as a function of $E-E_F$ where E is the energy of the HOMO level for each probe. The black points are experimental data obtained from Figure S9A, and the green curve is the fit to eq 5 with N_T = 201 and T_{eff} = 1882 K. The fitting results of the hole population *vs* energy obtained with 585 ± 18 nm and 607 ± 18 nm excitations are shown in Figure 5C and 5D, respectively. Unfortunately, the hot carrier energy information on other wavelengths (*e.g.*, 466 nm) was not accessible due to immeasurable low electrochemical signal for the probes with more negative HOMO values.

The value of N_T represents the total number of extracted photogenerated holes excited at a given wavelength. On the basis of the fits, we extract the highest number of holes when the excitation wavelength is resonant with the plasmon resonance of the substrate (N_T (607 nm) < N_T (562 nm) < N_T (585 nm)), in agreement with our wavelength dependent EQE values (Figure 3C). Our T_{eff} values fall between 1790 and 1882 K and are well within values suggested by theoretical calculations.[31] Moreover, the elevated T_{eff} values (well above the <1 K lattice temperature increase we expect due to photothermal heating)[37] indicate that our molecular probes are capturing and successfully extracting the plasmon-generated hot carriers before lattice thermalization. Interestingly, we also find that the trend of the effective carrier temperature increases with increasing photon energy (*e.g.*, T_{eff} (607 nm) < T_{eff} (585 nm) < T_{eff} (562 nm)). We expect that the highest energy photons will produce the highest energy hot carriers upon the initial excitation (*e.g.*, when t < 10 fs), and the temperatures we calculate here suggest that these higher energy carriers evolve to an effectively "hotter" distribution of extracted hot holes at longer time scale.

CONCLUSION

We have successfully quantified hot carrier energy distributions generated at metal/semiconductor nanostructures from the photoelectrochemical responses of a series of molecular redox probes. SECM allows us to probe the reaction kinetics and extract quantum efficiencies of the surface-plasmon-mediated photo-oxidation reactions at Au/TiO_2/ITO substrates. The redox probe dependent quantum efficiencies shed light on the energy distribution of the hot holes after the electron injection to the semiconductor layer. The experimentally obtained energy distributions are fit to the Fermi−Dirac distribution function, and the effective carrier temperatures during the initial carrier thermalization step are successfully extracted. The determined numbers of hot carriers and effective carrier temperatures are wavelength dependent, and the trends are consistent with the plasmon resonance spectrum and the photon energies, respectively. These results have implications for understanding the achievable quantum efficiencies of plasmonic photocatalytic devices. It is anticipated that more efficient plasmonic photocatalysts could be designed on the basis of the insights into hot carrier distributions at the plasmonic/semiconductor interfacial structure. We note that the devices described herein are not designed for maximum efficiency, given the amorphous nature of the semiconductor and the inherent heterogeneity of the deposited gold nanodiscs. Thus, with structure design optimization and creation of better metal/semiconductor interfaces, we expect that improved charge extraction efficiency and quantum efficiencies are possible.

METHODS

Chemicals. Potassium hexacyanoferrate (II) trihydrate ($K_4Fe(CN)_6 \cdot 3H_2O$, 99.95%), potassium ferricyanide ($K_3Fe(CN)_6$, 99%), ferrocenemethanol (FcMeOH, 97%), potassium hexachloroiridate-(III) (K_3IrCl_6), and potassium chloride (KCl, 99%) were purchased from Sigma-Aldrich and used as received. Ferrocenylmethyltrimethylammonium hexafluorophosphate ($FcTMAPF_6$) was prepared by metathesis of ferrocenylmethyltrimethylammonium iodide (FcTMAI, Alfa Aesar) with ammonium hexafluorophosphate (NH_4PF_6, 99.5%, Alfa Aesar) in water followed by filtration and drying under vacuum. All aqueous solutions were prepared using deionized water from the arium pro ultrapure water systems (Sartorius).

Substrate Preparation and Characterization. ITO-coated glass coverslips (15−30 Ω, SPI Supplies) were cleaned inside an

argon plasma cleaner (PDC-32G, Harrick Plasma) for 10 min. TiO_2 thin films were deposited onto the ITO surface from a ceramic TiO_2 target in a Pascal laser molecular beam epitaxy (MBE) system. A KrF excimer laser (λ = 248 nm, pulse duration 25 ns) with an energy density of 0.8 J/cm^2 was used to ablate the TiO_2 target. ~40 nm thick TiO_2 film is grown after 20 000 laser pulses with a repetition rate of 20 Hz at 300 °C. Gold (99.95%, Ted Pella) was thermally evaporated (Nano 36, Kurt J. Lesker) onto the TiO_2 surface at a rate of 0.5 Å/s to a final thickness of 10 nm. The deposited Au was annealed in air at 400 °C for 1 h. A Veeco Dimension atomic force microscope (AFM) and a FEI Quanta 450 FEG scanning electron microscope (SEM) were used to characterize the surface morphology of the substrate. The extinction spectrum of the Au film was collected with an UV−vis spectrophotometer (Ocean Optics).

SECM Setup. Pt disk UMEs were prepared by pulling and heat sealing 25-μm-diameter Pt wires (Goodfellow) into borosilicate glass capillaries with a P-2000 laser pipet puller (Sutter Instrument) and polishing under video microscopic control, as described previously.[37] All electrochemical measurements were performed using a CH750E bipotentiostat (CH Instruments). A Pt wire and an Ag wire coated with AgCl were used as a counter and reference electrode, respectively. The tip electrode was positioned close to the substrate using a stepper motor (Microdrive, Mad City Laboratories) and a piezo actuator (Thorlabs). The process is monitored with an inverted optical microscope (Olympus IX-73). The incident light was introduced from a laser-driven light source with spectral output from 190 to 2100 nm (EQ-99XFC, Energetiq Technology) to the bottom of the substrate through a 1.45 NA/60× oil immersion objective (Olympus). Band-pass filters (Edmund Optics) and neutral-density filters (Newport) were placed in the optical path to modulate the excitation wavelength and power, respectively. The light was chopped with an optical shutter (Uniblitz Electronic).

Finite-Element Simulation. The finite element simulations were performed using COMSOL Multiphysics v5.2a (COMSOL) to model the tip current response. Simulation details are provided in the Supporting Information.

ASSOCIATED CONTENT

Supporting Information

The Supporting Information is available free of charge on the ACS Publications website at DOI: 10.1021/acsnano.9b00219.

Characterization of TiO_2 and Au film, SECM data in generation-collection and feedback mode, action spectra of quantum efficiency, response from control groups, extinction spectrum of bare TiO_2 film, open-circuit potential measurement, UV−vis spectra of redox molecules, energy distribution obtained from other wavelengths, and descriptions of the finite-element simulation (PDF)

AUTHOR INFORMATION

Corresponding Author

*E-mail: kwillets@temple.edu.

ORCID

Yun Yu: 0000-0002-0204-1012

Katherine A. Willets: 0000-0002-1417-4656

Notes

The authors declare no competing financial interest.

ACKNOWLEDGMENTS

Y.Y. and K.A.W. acknowledge the support by the AFOSR MURI (FA9550-14-1-0003). K.W. and X.X.X. acknowledge the support by Center for the Computational Design of Functional Layered Materials, an Energy Frontier Research Center funded by the U.S. Department of Energy, Office of Science, Basic Energy Sciences under Award #DE-SC0012575. The authors thank Dr. V. Sundaresan, K. D. Rasamani, N. Molina, and J. Monaghan for their assistance in experiments and helpful discussions.

REFERENCES

(1) Zhang, Y.; He, S.; Guo, W.; Hu, Y.; Huang, J.; Mulcahy, J. R.; Wei, W. D. Surface-Plasmon-Driven Hot Electron Photochemistry. *Chem. Rev.* **2018**, *118*, 2927−2954.

(2) Christopher, P.; Xin, H.; Linic, S. Visible-Light-Enhanced Catalytic Oxidation Reactions on Plasmonic Silver Nanostructures. *Nat. Chem.* **2011**, *3*, 467−472.

(3) Linic, S.; Christopher, P.; Ingram, D. B. Plasmonic-Metal Nanostructures for Efficient Conversion of Solar to Chemical Energy. *Nat. Mater.* **2011**, *10*, 911−921.

(4) Kale, M. J.; Avanesian, T.; Christopher, P. Direct Photocatalysis by Plasmonic Nanostructures. *ACS Catal.* **2014**, *4*, 116−128.

(5) Brooks James, L.; Warkentin Christopher, L.; Saha, D.; Keller Emily, L.; Frontiera Renee, R. Toward a Mechanistic Understanding of Plasmon-Mediated Photocatalysis. *Nanophotonics* **2018**, *7*, 1697−1724.

(6) Linic, S.; Aslam, U.; Boerigter, C.; Morabito, M. Photochemical Transformations on Plasmonic Metal Nanoparticles. *Nat. Mater.* **2015**, *14*, 567−576.

(7) Narang, P.; Sundararaman, R.; Atwater Harry, A. Plasmonic Hot Carrier Dynamics in Solid-State and Chemical Systems for Energy Conversion. *Nanophotonics* **2016**, *5*, 96−111.

(8) Marchuk, K.; Willets, K. A. Localized Surface Plasmons and Hot Electrons. *Chem. Phys.* **2014**, *445*, 95−104.

(9) Christopher, P.; Moskovits, M. Hot Charge Carrier Transmission from Plasmonic Nanostructures. *Annu. Rev. Phys. Chem.* **2017**, *68*, 379−398.

(10) Brongersma, M. L.; Halas, N. J.; Nordlander, P. Plasmon-Induced Hot Carrier Science and Technology. *Nat. Nanotechnol.* **2015**, *10*, 25−34.

(11) Brandt, N. C.; Keller, E. L.; Frontiera, R. R. Ultrafast Surface-Enhanced Raman Probing of the Role of Hot Electrons in Plasmon-Driven Chemistry. *J. Phys. Chem. Lett.* **2016**, *7*, 3179−3185.

(12) Clavero, C. Plasmon-Induced Hot-Electron Generation at Nanoparticle/Metal-Oxide Interfaces for Photovoltaic and Photocatalytic Devices. *Nat. Photonics* **2014**, *8*, 95−103.

(13) Tian, Y.; Tatsuma, T. Mechanisms and Applications of Plasmon-Induced Charge Separation at TiO2 Films Loaded with Gold Nanoparticles. *J. Am. Chem. Soc.* **2005**, *127*, 7632−7637.

(14) Wang, S.; Gao, Y.; Miao, S.; Liu, T.; Mu, L.; Li, R.; Fan, F.; Li, C. Positioning the Water Oxidation Reaction Sites in Plasmonic Photocatalysts. *J. Am. Chem. Soc.* **2017**, *139*, 11771−11778.

(15) Qian, K.; Sweeny, B. C.; Johnston-Peck, A. C.; Niu, W.; Graham, J. O.; DuChene, J. S.; Qiu, J.; Wang, Y.-C.; Engelhard, M. H.; Su, D.; Stach, E. A.; Wei, W. D. Surface Plasmon-Driven Water Reduction: Gold Nanoparticle Size Matters. *J. Am. Chem. Soc.* **2014**, *136*, 9842−9845.

(16) Gomes Silva, C.; Juárez, R.; Marino, T.; Molinari, R.; García, H. Influence of Excitation Wavelength (UV or Visible Light) on the Photocatalytic Activity of Titania Containing Gold Nanoparticles for the Generation of Hydrogen or Oxygen from Water. *J. Am. Chem. Soc.* **2011**, *133*, 595−602.

(17) Mubeen, S.; Lee, J.; Singh, N.; Kramer, S.; Stucky, G. D.; Moskovits, M. An Autonomous Photosynthetic Device in Which All Charge Carriers Derive from Surface Plasmons. *Nat. Nanotechnol.* **2013**, *8*, 247−251.

(18) Lee, J.; Mubeen, S.; Ji, X.; Stucky, G. D.; Moskovits, M. Plasmonic Photoanodes for Solar Water Splitting with Visible Light. *Nano Lett.* **2012**, *12*, 5014−5019.

(19) Hou, W.; Hung, W. H.; Pavaskar, P.; Goeppert, A.; Aykol, M.; Cronin, S. B. Photocatalytic Conversion of CO2 to Hydrocarbon Fuels *via* Plasmon-Enhanced Absorption and Metallic Interband Transitions. *ACS Catal.* **2011**, *1*, 929−936.

(20) Robatjazi, H.; Zhao, H.; Swearer, D. F.; Hogan, N. J.; Zhou, L.; Alabastri, A.; McClain, M. J.; Nordlander, P.; Halas, N. J. Plasmon-Induced Selective Carbon Dioxide Conversion on Earth-Abundant Aluminum-Cuprous Oxide Antenna-Reactor Nanoparticles. *Nat. Commun.* **2017**, *8*, 27.
(21) Tsukamoto, D.; Shiraishi, Y.; Sugano, Y.; Ichikawa, S.; Tanaka, S.; Hirai, T. Gold Nanoparticles Located at the Interface of Anatase/Rutile TiO2 Particles as Active Plasmonic Photocatalysts for Aerobic Oxidation. *J. Am. Chem. Soc.* **2012**, *134*, 6309−6315.
(22) Hao, C.-H.; Guo, X.-N.; Pan, Y.-T.; Chen, S.; Jiao, Z.-F.; Yang, H.; Guo, X.-Y. Visible-Light-Driven Selective Photocatalytic Hydrogenation of Cinnamaldehyde over Au/SiC Catalysts. *J. Am. Chem. Soc.* **2016**, *138*, 9361−9364.
(23) Murdoch, M.; Waterhouse, G. I. N.; Nadeem, M. A.; Metson, J. B.; Keane, M. A.; Howe, R. F.; Llorca, J.; Idriss, H. The Effect of Gold Loading and Particle Size on Photocatalytic Hydrogen Production from Ethanol over Au/TiO2 Nanoparticles. *Nat. Chem.* **2011**, *3*, 489−492.
(24) Nishijima, Y.; Ueno, K.; Yokota, Y.; Murakoshi, K.; Misawa, H. Plasmon-Assisted Photocurrent Generation from Visible to near-Infrared Wavelength Using a Au-Nanorods/TiO2 Electrode. *J. Phys. Chem. Lett.* **2010**, *1*, 2031−2036.
(25) Furube, A.; Du, L.; Hara, K.; Katoh, R.; Tachiya, M. Ultrafast Plasmon-Induced Electron Transfer from Gold Nanodots into TiO2 Nanoparticles. *J. Am. Chem. Soc.* **2007**, *129*, 14852−14853.
(26) Ratchford, D. C.; Dunkelberger, A. D.; Vurgaftman, I.; Owrutsky, J. C.; Pehrsson, P. E. Quantification of Efficient Plasmonic Hot-Electron Injection in Gold Nanoparticle−TiO2 Films. *Nano Lett.* **2017**, *17*, 6047−6055.
(27) Ng, C.; Cadusch, J. J.; Dligatch, S.; Roberts, A.; Davis, T. J.; Mulvaney, P.; Gómez, D. E. Hot Carrier Extraction with Plasmonic Broadband Absorbers. *ACS Nano* **2016**, *10*, 4704−4711.
(28) Schlather, A. E.; Manjavacas, A.; Lauchner, A.; Marangoni, V. S.; DeSantis, C. J.; Nordlander, P.; Halas, N. J. Hot Hole Photoelectrochemistry on Au@SiO2@Au Nanoparticles. *J. Phys. Chem. Lett.* **2017**, *8*, 2060−2067.
(29) Manjavacas, A.; Liu, J. G.; Kulkarni, V.; Nordlander, P. Plasmon-Induced Hot Carriers in Metallic Nanoparticles. *ACS Nano* **2014**, *8*, 7630−7638.
(30) Sundararaman, R.; Narang, P.; Jermyn, A. S.; Goddard Iii, W. A.; Atwater, H. A. Theoretical Predictions for Hot-Carrier Generation from Surface Plasmon Decay. *Nat. Commun.* **2014**, *5*, 5788.
(31) Saavedra, J. R. M.; Asenjo-Garcia, A.; García de Abajo, F. J. Hot-Electron Dynamics and Thermalization in Small Metallic Nanoparticles. *ACS Photonics* **2016**, *3*, 1637−1646.
(32) Heilpern, T.; Manjare, M.; Govorov, A. O.; Wiederrecht, G. P.; Gray, S. K.; Harutyunyan, H. Determination of Hot Carrier Energy Distributions from Inversion of Ultrafast Pump-Probe Reflectivity Measurements. *Nat. Commun.* **2018**, *9*, 1853.
(33) Haram, S. K.; Bard, A. J. Scanning Electrochemical Microscopy. 42. Studies of the Kinetics and Photoelectrochemistry of Thin Film CdS/Electrolyte Interfaces. *J. Phys. Chem. B* **2001**, *105*, 8192−8195.
(34) Lhenry, S.; Boichard, B.; Leroux, Y. R.; Even-Hernandez, P.; Marchi, V.; Hapiot, P. Photo-Electrochemical Properties of Quantum Rods Studied by Scanning Electrochemical Microscopy. *Phys. Chem. Chem. Phys.* **2017**, *19*, 4627−4635.
(35) Conzuelo, F.; Sliozberg, K.; Gutkowski, R.; Grützke, S.; Nebel, M.; Schuhmann, W. High-Resolution Analysis of Photoanodes for Water Splitting by Means of Scanning Photoelectrochemical Microscopy. *Anal. Chem.* **2017**, *89*, 1222−1228.
(36) Zhou, X.; Gossage, Z. T.; Simpson, B. H.; Hui, J.; Barton, Z. J.; Rodríguez-López, J. Electrochemical Imaging of Photoanodic Water Oxidation Enhancements on TiO2 Thin Films Modified by Subsurface Aluminum Nanodimers. *ACS Nano* **2016**, *10*, 9346−9352.
(37) Yu, Y.; Sundaresan, V.; Willets, K. A. Hot Carriers versus Thermal Effects: Resolving the Enhancement Mechanisms for Plasmon-Mediated Photoelectrochemical Reactions. *J. Phys. Chem. C* **2018**, *122*, 5040−5048.
(38) Yu, Y.; Williams, J. D.; Willets, K. A. Quantifying Photothermal Heating at Plasmonic Nanoparticles by Scanning Electrochemical Microscopy. *Faraday Discuss.* **2018**, *210*, 29−39.
(39) Bard, A. J.; Faulkner, L. R. *Electrochemical Methods: Fundamentals and Applications*, 2nd ed.; Wiley: New York, 2001.
(40) Lei, Q.; Golalikhani, M.; Davidson, B. A.; Liu, G.; Schlom, D. G.; Qiao, Q.; Zhu, Y.; Chandrasena, R. U.; Yang, W.; Gray, A. X.; Arenholz, E.; Farrar, A. K.; Tenne, D. A.; Hu, M.; Guo, J.; Singh, R. K.; Xi, X. Constructing Oxide Interfaces and Heterostructures by Atomic Layer-by-Layer Laser Molecular Beam Epitaxy. *NPJ. Quan. Mater.* **2017**, *2*, 10.
(41) Yu, Y.; Sun, T.; Mirkin, M. V. Toward More Reliable Measurements of Electron-Transfer Kinetics at Nanoelectrodes: Next Approximation. *Anal. Chem.* **2016**, *88*, 11758−11766.
(42) Bian, Z.; Tachikawa, T.; Zhang, P.; Fujitsuka, M.; Majima, T. Au/TiO2 Superstructure-Based Plasmonic Photocatalysts Exhibiting Efficient Charge Separation and Unprecedented Activity. *J. Am. Chem. Soc.* **2014**, *136*, 458−465.
(43) Scanlon, M. D.; Peljo, P.; Méndez, M. A.; Smirnov, E.; Girault, H. H. Charging and Discharging at the Nanoscale: Fermi Level Equilibration of Metallic Nanoparticles. *Chem. Sci.* **2015**, *6*, 2705−2720.
(44) Li, Y.; Bergman, D.; Zhang, B. Preparation and Electrochemical Response of 1−3 nm Pt Disk Electrodes. *Anal. Chem.* **2009**, *81*, 5496−5502.
(45) Watkins, J. J.; Chen, J.; White, H. S.; Abruña, H. D.; Maisonhaute, E.; Amatore, C. Zeptomole Voltammetric Detection and Electron-Transfer Rate Measurements Using Platinum Electrodes of Nanometer Dimensions. *Anal. Chem.* **2003**, *75*, 3962−3971.